Digital design and 3D printing of innovative SiC architectures for high temperature volumetric solar receivers

Cyprien Heisel, Cyril Caliot, Thierry Chartier, Sylvain Chupin, Patrick David, Denis Rochais

Digital design and 3D printing of innovative SiC architectures for high temperature volumetric solar receivers

HEISEL Cyprien[a], CALIOT Cyril[b,c], CHARTIER Thierry[d], CHUPIN Sylvain[a], DAVID Patrick[a], ROCHAIS Denis[a]

[a]CEA, DAM, LE RIPAULT, F-37260 Monts, France
[b]Université de Pau et des Pays de l'Adour, E2S UPPA, CNRS, LMAP, Anglet, France
[c]Processes, Materials and Solar Energy Laboratory (CNRS-PROMES), 7 rue du Four Solaire – 66120 Font-Romeu, France
[d]CNRS, University of Limoges, Institute of Research for Ceramics (IRCER), European Ceramics Center, Limoges, France

Corresponding author: ROCHAIS Denis (denis.rochais@cea.fr)

Abstract

In order to demonstrate that digital material engineering methodology is able to address the design and optimisation of architectured ceramic materials, solar volumetric receivers employed in Solar Thermal Power Plants (STPP) have been studied. A digital design approach for obtaining new receivers, at the macroscopic structural scale, is proposed. This approach couples virtual structure generation, ray tracing and thermal simulations at the scale of the base structural components (microscopic scale). Then, a recently developed process for manufacturing silicon carbide (SiC) parts by binder jetting is used to elaborate three optimised structures which are tested on-sun at high temperature in a solar concentrator reproducing the STPP operation conditions. The results obtained with these structures, having original shapes, are promising: the average experimental outlet air temperature reaches a maximum of 1133 K, energy yields can reach 0.49 despite high experimental heat losses, and all the SiC structures, made with a new material based on 3D printing, withstood the high temperatures reached, up to 1500 K. Comparison between digital and experimental results shows that the approach presented in this paper paves the way to a new digital material engineering approach.

Keywords: SiC, binder jetting, solar volumetric receiver, ray tracing, conductive radiative heat transfer, high temperature.

1. Introduction

Experimental characterisation of some materials, when they have particular characteristics (complex microstructure and/or architecture, significant brittleness, small dimensions, etc.), is very delicate, sometimes even impossible. The objective set by the digital materials approach, developed at CEA Le Ripault over the past fifteen years [1], is to perform these experiments numerically. For this purpose, the real material is digitised or voxelised using 3D image reconstruction means (X-ray tomography,

FIB/SEM, for example). Then, using the intrinsic properties of the material components and numerical tools to simulate physical phenomena, digital experiments can be used to study the coupled heat and mass transfers, and to develop approximate models with their effective properties of the equivalent material based on the detailed virtual structure.

Recent advances [2,3] in additive manufacturing processes now allow this approach to be extended to the digital engineering of materials. The idea is to start with a virtual material and optimise it by calculation to meet specifications as precisely as possible, and then to manufacture this customed material by 3D printing. The objective of this article is to implement digital material engineering methodology and to demonstrate that this innovative approach is relevant.

To this end, the study of high temperature volumetric receivers [4–8] of Solar Thermal Power Plants (STPP) has been selected. These receivers, integrated at the top of a solar tower, are used to absorb energy from the Sun's rays, concentrated via numerous heliostats. Then, a heat transfer fluid (atmospheric air or pressurised air) [9,10] can flow through their 3D, macroporous architecture to recover the captured solar energy. A high temperature thermodynamic system installed in the power plant enables the recovered thermal energy to be converted at high efficiency.

In this type of receiver, the challenge consists in designing a receiver achieving the volumetric effect which would result in a drastic increase in the thermal efficiency of the receiver (defined as the ratio of the energy provided by the incident solar flux over the energy recovered by the heat transfer fluid) [11]. This effect is characterised by two essential points depicted in Figure 1. The first point is an absorber (solid part of the receiver) temperature that is lower at the inlet than at the outlet – labelled "Exit" in Figure 1 – (limiting thermal losses by radiation towards the environment), and the second point is an elevated outlet fluid temperature (typically 1200 K) which can be used in high efficiency thermodynamic cycles.

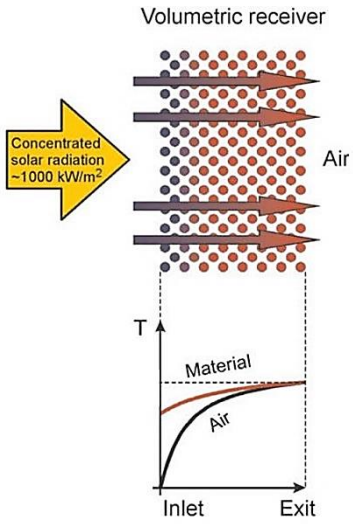

Figure 1: Temperature profile in a volumetric receiver, showing the volumetric effect [12].

The materials used for these receivers are divided into two families [13]. They are either metallic or ceramic. In the first case, the absorbers are more resistant to thermal shocks induced by fluctuations in the incident solar flux, but the maximum temperatures reached cannot exceed approximately 1100 K (due to the risk of the metal melting or rusting), thus limiting the power released by the STPP. Ceramic absorbers are, on the contrary, more resistant to high temperatures [14]. Ceramic absorbers,

which are more promising, are the subject of our study. Silicon carbide (SiC), the reference material for this solar application [4,15,16], is known for its refractory nature and its high absorption in the solar radiation wavelength spectrum. In this respect, SiC has been selected in this study.

The heat transfer fluid can be used pressurised or at atmospheric pressure. In theory, when the fluid is pressurised, the energy yields of the receivers are greater [17,18] but the design of the window, which keeps the fluid circuit closed while allowing the Sun's rays to pass through, is very difficult to achieve [19,20]. Finally, the advantage of receivers at atmospheric pressure is their lower cost due to their less complex implementation. The family of ceramic absorbers used at atmospheric pressure was therefore preferred for our study.

Due to manufacturing considerations, the geometries of SiC receivers are mainly foams and honeycombs. Honeycombs may be more sensitive to incident solar radiation heterogeneity (hot spots) compared to foams [17,21], which have been widely studied experimentally [4,16,22,23] and numerically [24–26]. Foams used as atmospheric air solar receivers present a major drawback, they absorb the solar flux in the first part of their depth (5 to 10 %), not exploiting the full potential of the specific surface area they offer. Nevertheless, some experimental [27] and numerical studies tend to demonstrate that the volumetric effect may be possible to achieve, but important geometric or physical considerations have to be taken into account [25,26,28].

The search for new geometries in SiC is therefore the key to improve the performance of volumetric receivers, and additive manufacturing is a technological solution making it possible to manufacture these new morphologies. Recent studies have shown how to do this and have proposed new 3D printed complex ceramic geometries, most of them 3D lattices structures in alumina, zirconia, Si-SiC or SiOC-SiC [29–32].

To our knowledge, two methods have been used to build 3D ceramics parts: stereolithography of Polymer Derived Ceramics (PDC) and binder jetting [33]. In both cases, post-treatments are necessary to obtain a rather dense final ceramic part. [34–38] recently reported printed Si-SiC or SiOC structures, using the stereolithography process associated with pre-ceramic polymers. After thermal post-treatments, the final parts are dense without cracks and have a good surface finish. This thermal treatment leads to high linear shrinkage (i.e. greater than 25%) according to the ceramisation yield of the prepolymer, which is about 60%. [39–41] used the binder jetting technique to print various cellular structures. The linear shrinkage of the parts obtained, after post-treatments, is between 1 and 20%, depending on the printing parameters and on the residual internal porosity, which can reach 40%.

In this work, the digital material approach described above is applied with the help of a modified process [2] which makes it possible to manufacture, by binder jetting, complex parts in SiC, with a minimum resolution of approximately 700 microns. After digital optimization of morphologies, thermal simulations are carried out on these structures to evaluate their performances. Then they are printed and experimental tests are carried out in order to compare the real behaviours with the virtual ones. This work proposes and validates an approach which consists in numerically determining the best morphology for a volumetric receiver and then to manufacture it in SiC. Furthermore, the 3D printer used in this work enables parts to be manufactured with dimensions up to 20 cm, such as modules used in the construction of volumetric receivers.

The first part of this article concerns a description of the manufacture of a 3D binder jetting printer and the on-sun test bench with solar concentration. Then, in a second part, the approach followed to optimise and create new geometries for volumetric receivers is detailed. The third part is devoted to the description of the digital tools employed. The fourth part presents the various numerical and experimental results. Finally, some conclusions and perspectives are given.

2. General approach

The desired ceramic material with optimised shaping for volumetric receptors is achieved through a strategy combining numerical and experimental steps (Figure 2).

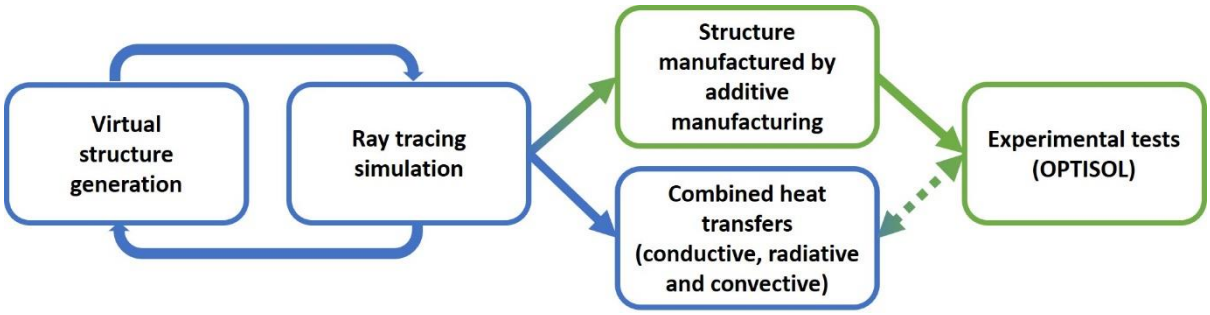

Figure 2: Diagram of the approach followed. In blue: digital steps. In green: experimental steps. Dotted line: results comparison.

In order to determine an optimal shape, we used two computation codes. The first was a virtual generating code, and the second was a ray tracing code. These two codes are closely linked since an optimisation loop is formed between them.

Firstly, a structure is generated which follows the specifications from the literature. These are: i) to absorb the incident solar flux as uniformly as possible according to its depth [16,42–44], presenting very few absorptions skips to avoid thermal-mechanical stresses; ii) to limit reflective losses on the front face [43,45]; iii) to capture the entire solar flux. Finally, these specifications can result in a curve, shown in Figure 3, which is the dimensionless transmission of the incident solar flux as a function of the depth of the receiver. This curve is linear (no absorption skips), decreasing (uniform absorption), starts from 1 (no losses on the front face) and ends at 0 (all of the solar flux is absorbed). This “ideal” curve is the reference for judging the solar absorption performance of the developed structures.

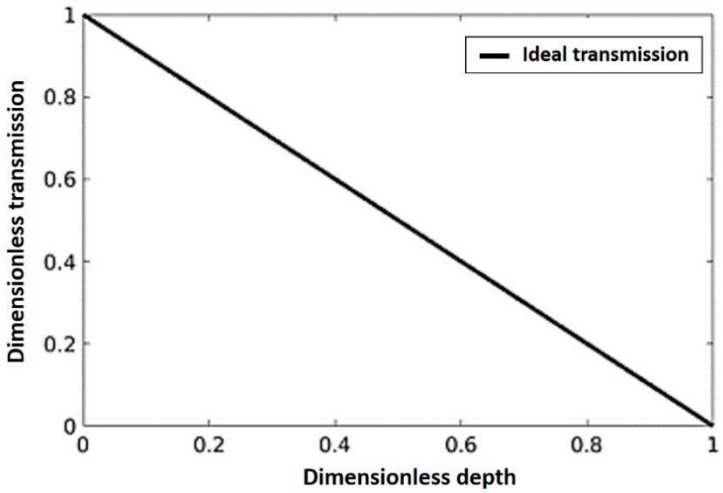

Figure 3: "Ideal" transmission describing our specifications. The transmission is rendered dimensionless relative to the incident solar flux and the depth is rendered dimensionless relative to the total length of the receiver.

Next, a ray tracing simulation is performed. The transmissivity results are compared with the ideal curve. If it is satisfactory, the structure is retained and the next steps can be started. Otherwise, the initial virtual structure is modified, or a new structure is generated, until a satisfactory result is obtained. To do so, a criterion Λ has been defined as the product of four quantities defined below:

$$\Lambda = \Lambda_{abs} * \Lambda_{skips} * \Lambda_{refl} * \Lambda_{trans} \quad (1)$$

Where Λ_{abs}, Λ_{skips}, Λ_{refl} and Λ_{trans} allow to evaluate the deviations to the specifications mentioned above, corresponding respectively to the uniformity of absorption, to the absorption skips, to the reflective losses and to the losses by transmissivity. These quantities, comprising between 0 and 1 are calculating by the following formulas:

$$\Lambda_{abs} = 1 - \frac{\sum_{i=1}^{n} |T(i) - T_{ideal}(i)|}{\sum_{i=1}^{n} T_{ideal}(i)} \quad (2)$$

$$\Lambda_{skips} = \frac{1 - max(|T(i) - T(i+1)|)}{1 - max(|T_{ideal}(i) - T_{ideal}(i+1)|)} \quad (3)$$

$$\Lambda_{refl} = 1 - \frac{Q_{r,front}}{Q_0} \quad (4)$$

$$\Lambda_{trans} = 1 - T(n) \quad (5)$$

Where $T(i)$ is the value of transmissivity calculated in the structure at the ith slice (see formula 7 in section 4.2.1), $T_{ideal}(i)$ is the ideal transmissivity at the same ith slice and n is the total number of slice. $Q_{r,front}$ is the reflective losses the front face, calculated during code execution, and Q_0 is the solar radiative flux of the light source. The calculation of Λ gives a value, comprising between 0 and 1 and the more this value is close to 1, the more the structure is considered to satisfying the specifications. To reach the higher possible value of Λ, modifications of the initial virtual structure can be made, for example, variations in the strut thickness or a rotation of this structure in space (modification of the impact of the solar flux incidence).

Figure 4 shows an example of an original structure, where the criterion is equal to 0.54, and an optimised structure, obtained after a rotation in space, and with a criterion equal to 0.70. The growth

of the criterion is due to a better absorption on space and lower absorption skips. Nevertheless, the criterion is not closer to 1 because the losses by reflectivity on the front face and the transmissivity on the rear face are high.

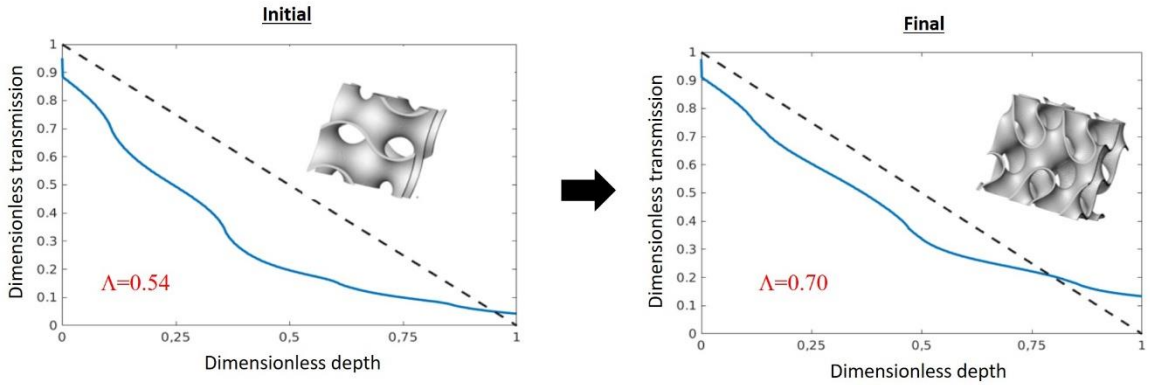

Figure 4: Example of an optimization of a structure. On the right, the original structure and on the right, the final structure. Black curve is the ideal transmission and blue curve is the transmission in each structure.

Each step of the loop (generation/modification of the structure, calculation of the transmission and calculation of the criterion) is carried out automatically but their sequence is done manually. One iteration of the loop takes some minutes (a few seconds for the generation of the structure and about twenty minutes for the ray tracing code).

After the numerical loop, the optimised structures are manufactured by 3D printing (binder jetting) and then evaluated in the solar test bench (OPTISOL) [16] that reproduces, at the laboratory scale, the conditions to which a high temperature solar volumetric receiver is subjected.

Finally, a digital step is carried out in parallel with the manufacturing and experimental tests. The flux absorbed by the material structure is computed by ray tracing and included in a simulation of the combined heat transfers. This code simulates the coupled conduction and radiation heat transfers, in one hour approximatively on a 32 processor calculator. The fluid dynamics are not solved but a constant convective heat transfer coefficient throughout the volume is considered. Once the stationary regime is reached, a temperature field in the structure is established. Numerical outlet air temperatures of the structures can thus be compared with the experimental results.

Two major simplifications were adopted in this approach.

The first concerns the approximation of the convective heat transfer with a coefficient instead of solving the coupled fluid dynamics. The integration of a fluid dynamics code in the process would have been computationally demanding.

The second simplification is the selection of structures after the loop on structure generation and ray tracing (Figure 2). The ideal methodology would have been to choose the structures after having carried out an optimisation loop on all the digital steps (blue cells in Figure 2). This option was not selected because the heat transfer model was not considered precise enough due to the approximation on the convection heat transfer.

Moreover, this simplification was made in our study because the distribution of the absorbed solar energy and the specific surface area are considered the key parameters to maximise the energy efficiency of the volumetric receiver [16,25,42,43,45].

3. Experimental tools and methods

3.1 3D printing

The manufacturing process of SiC structures with complex shapes consists of two major stages [2]. The first stage is the printing of the part in its final shape using a binder jetting 3D printer (ZPrinter 310+ from ZCorporation, USA). The porous part thus obtained with low cohesion, which is called "raw", is then subjected to different treatments in order to obtain the desired dense and cohesive SiC structure. These post-processing treatments constitute the second major stage of the process used.

The raw part is obtained from a mixture of SiC powder (d_{50}=25µm, Sigma-Aldrich) and plaster powder (d_{50}=25µm, ZCorp), with a SiC/plaster ratio of 56/44 wt%. The binder (ZCorp) is sprayed by a nozzle moving in the XY plane, to consolidate a 100 µm deposited layer of a SiC/plaster powder in the defined cross-sectional pattern. The deposition of a SiC/plaster powder layer and its consolidation by jetting of binder is repeated until completion of the raw part. The cohesion of the raw part is ensured by the plaster, which binds the SiC particles together, but the raw part remains brittle.

In order to obtain a final dense SiC part, several post-treatments were carried out. Firstly, the raw part was immersed in a solution of SiC precursor (SMP-10, Starfire, USA) diluted in toluene (toluene/SMP-10 = 40 wt%), in air and at room temperature, in order to impregnate the porous raw part with SiC. The SMP-10 precursor was chosen because it is liquid at room temperature, it easily infiltrates the porous structure and because it allows a high ceramisation rate (greater than 70%) [46–48]. Then, the part was heated to 250°C in air for one hour (with a heating rate of 100°C/hour), then cooled down to room temperature (cooling rate of 100°C/hour). This stage makes it possible to polymerise the precursor and therefore to consolidate the raw part with a SiC (ex-precursor) lattice. A second heat treatment is then carried out at 1000°C for two hours under argon (with an increase and decrease rate of 100°C/hour). This pyrolysis makes it possible to ceramise the precursor [46,49]. In order to ensure good cohesion of the part at this stage, the plaster still contained in the part can then be removed by immersing the part in a hydrochloric acid bath at 50°C, in air, for four hours. This chemical removal of the plaster leaves microporosity within the part, which is further partially filled by Chemical Vapour Infiltration (CVI). Finally, a subsequent reinforcement was performed by Chemical Vapour Deposition (CVD), to also fill a part of the microporosity, and mostly to create a solid skeleton of a few tens of microns around the part. All these treatments (SMP-10 infiltration, CVI, CVD) reinforce the material and improve its properties (thermal, mechanical, resistance to rusting, etc.). A complex material, composed of several types of SiC, is thus obtained. This material, a cross section of which is shown in Figure 5, was observed in a previous study [50]. In this same study, the conditions of these last two reinforcements, as well as details regarding the manufacturing stages, are detailed.

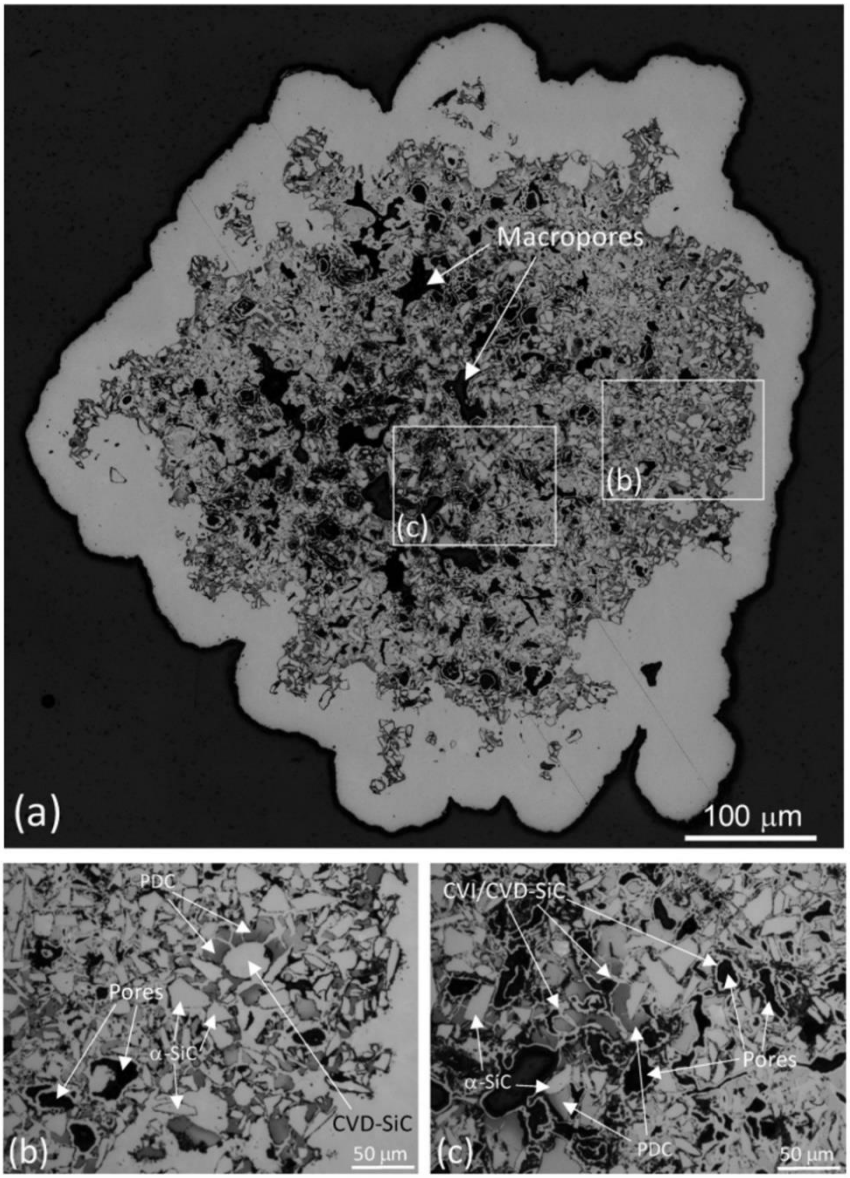

Figure 5: Cross-section of a sample after all treatments (SMP-10 infiltration, CVI, CVD). α-Sic is the SiC powder and PDC is the SiC from the SMP-10 precursor (from [50]*).*

3.2 OPTISOL: on-sun test bench

3.2.1 Solar facility

The experimental device of the PROMES laboratory (CNRS, Odeillo, France) is divided into two parts. A small solar facility allows the solar flux to be concentrated and directed towards the OPTISOL test bench used to characterise samples of high temperature solar volumetric receivers.

Figure 6 shows the two parts. Sun rays are reflected by a 27m² heliostat towards a dish concentrator, after passing through a hatch. This is the "6 kW" solar facility at the PROMES laboratory. The dish is composed of 306 hexagonal facets, all oriented towards a focal point, making a total surface area of 13.45 m². Once the solar rays are reflected on this surface, they are concentrated conically towards the OPTISOL test bench, with a half angle of 30°.

Figure 6: The two parts constituting the experimental device. On the left, the heliostat and the hatch and, on the right, the OPTISOL test bench held by a mechanical arm (in grey) and the concentrator (above). The photographs were taken from [16].

3.2.2 OPTISOL test bench

The purpose of the OPTISOL test bench [16] is to characterise the conversion efficiency of a concentrated solar flux into sensible heat transported by a high temperature atmospheric air flow thanks to a high temperature volumetric receiver. It consists of a fixed part and three interchangeable parts, depending on the type of measurement to be made.

The fixed part includes the following elements:

- A shutter, composed of eight fins, allowing the incident solar flux to be modulated,
- A glass flask, transparent to solar radiation, to separate the ambient air and the air injected into the system,
- A flow meter and a pressure sensor, to control the injected air flow,
- A homogeniser, to render the incident solar flux spatially uniform,
- A 5 cm diameter diaphragm, mounted on the homogeniser,
- Cooling water supplies for components exposed to the direct or overflowing solar flux,
- An infrared camera to measure the temperature distribution at the volumetric receiver inlet.

The interchangeable parts are:

- A cooled plate covered with a layer of magnesia to serve as a reflecting target in order to deduce the spatial distribution of the solar flux on the sample,
- A cooled black cavity, used as a calorimeter to deduce the value of the concentrated solar flux incident on the sample,
- An insulated sample holder with an outlet for the heated air flow, including thermocouples to measure the temperature of the volumetric receiver on its rear face.

3.2.3 Characterisation of samples

After the characterisation of the solar flux incident on the porous sample, the sample holder is inserted on the interchangeable part. The characterisation takes place in the following way. The hatch opens

to let the solar flux illuminate the dish. This solar flux, initially oriented by a heliostat, is reflected on the "6 kW" dish and passes through the glass flask to irradiate the front face of the samples. The air, separated from the ambient air by the glass flask, then circulates in the sample, from the front face to the rear face. Its flow is controlled using a mass flow controller. Thermocouples in contact with the rear face of the SiC sample measure its temperature, which can be associated with the fluid temperature if thermal equilibrium between the solid and fluid phases is reached. By measuring the incident solar flux, it is then possible to obtain an energy yield for the sample. More details about the test bench and about the associated solar flux measurements can be found in [16].

4 Digital tools

4.1 Generation of virtual structures

The virtual structures were all discretised into cubic voxels, where each is representative of the constituent of the medium it represents. The material properties were considered to be homogeneous in each voxel.

In addition, in order to being able to work on the digitised structures obtained from experimental characterisation (X-ray tomography, FIB / SEM), idealised structures with very varied shapes can also be digitally generated. We classified all of the digital structures into two large families: "random" and "organised" structures.

The so-called “random” structures correspond to those in which the solid skeleton of the virtual structure is constructed through random laws. This is the case in particular of foams generated by sphere growth, the position and radius of which are determined by normal or uniform laws, or even by fibrous media, represented by cylinders with random or pseudo-random orientations.

The so-called “organised” structures are, in contrast to “random” structures, all those in which the solid skeleton of the virtual structure is constructed in a deterministic way. This is the case of foams generated by duplication of an elementary pattern (Kelvin cell, for example), structures based on simple geometric shapes (cylinder, cone, sphere, etc.) and whose geometric parameters, position and orientation are defined exactly, or structures based on surface equations (Figure 7).

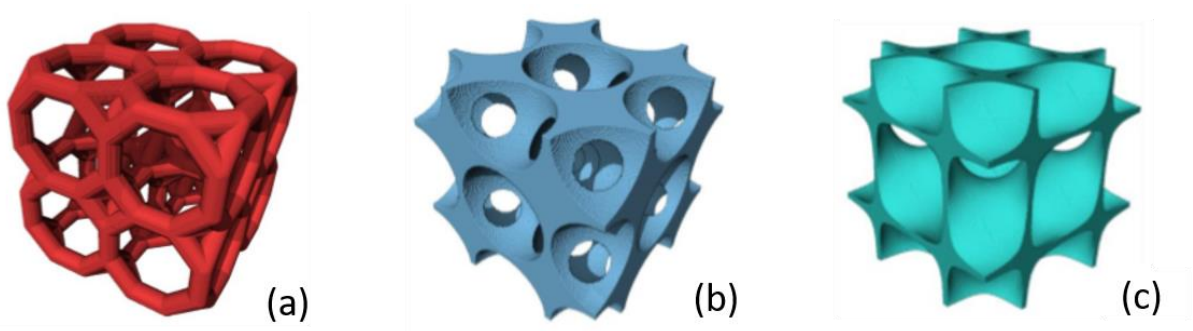

Figure 7: Examples of "organised" and periodic structures that we can generate. (a) Trellis-type honeycomb structure. (b) Structure with sphere growth arranged in a Cartesian layout in space. (c) Structure resulting from a surface equation.

For these two families of virtual structures it is possible to adjust one or more parameters (radius, number of elementary objects, for example) in order to regulate the porosity and/or the volume

surface. Finally, the digital tools described allow us to design a multitude of digital structures with a wide range of geometries.

4.2 Ray tracing

4.2.1 Computing code

The computing code developed makes it possible to model the energy distribution in a voxelised structure with solar rays starting from one of its faces. Several million digital rays are generated. Their initial starting point is located on the front face of the receiver and their initial direction is determined by a pair of angles from the spherical coordinates system. All of the rays are evenly dispersed on the front face (Cartesian section). The possible heterogeneity of the light source is considered by the energy transported by each ray, which can be different depending on the position where it is located on this front face.

A ray begins its path on the front face and propagates linearly within the volume. As soon as it meets a voxel representing the solid wall, this voxel absorbs part of the energy of the ray, depending on the absorptivity of the material represented by the voxel. The rest of the energy is transported by a new ray whose initial position becomes that of the affected voxel. The direction of this new ray (represented by a new pair of angles) is calculated using the Snell-Descartes law; the normal to each wall voxel is determined by a preliminary calculation, consisting in applying respectively a Gaussian blur and a Sobel filter over the entire structure. Then, the propagation of the new ray takes place in the same way as previously.

In addition, if a ray reaches one of the six edges of the domain, then boundary conditions apply. In the event of a periodic condition, the exiting ray is then replaced on the opposite edge with the same energy and the same direction. In the case of a "free" condition, the ray leaves the domain and it is no longer processed: the energy that it carries is added to that of all of the other rays having exited through this face. In this way, it is easy to determine energy losses through reflection (ray having exited through the front face) and through transmission (ray having exited through the rear face).

Once the simulation has ended, a loop traversing all of the voxels is made in order to count the energy recovered by each voxel. In the case of a homogeneous source (with solar radiative flux Q_0), the solar radiative flux $Q(i)$ of the incident flux transmitted throughout the depth of the structure is deduced using the following formula:

$$Q(i) = Q_0 \left(1 - \sum_{p=1}^{i} A(p) - Q_{r,front} \right) \qquad 6$$

where i is the index of the layer depth, $A(p)$ is the absorption of the slice p (deduced by adding the energy of each voxel included in this slice) and $Q_{r,front}$ is the value of the losses on the front face. The transmissivity at each slice i, $T(i)$ is deduced by the formula:

$$T(i) = \frac{Q(i)}{Q_0} \qquad 7$$

4.2.2 Simulation assumptions

This computing code was developed respecting the following assumptions:

1- Part of the energy of a ray striking a wall voxel is absorbed and another part is reflected. No part of this energy is transmitted, because of the strong absorptivity of the SiC material in the solar radiation wavelength spectrum and associated photon extinction after only a few tens of nanometres. Considering the size of the voxels used in this study (50 µm minimum), transmission is therefore negligible.
2- Since the manufactured SiC material has strong absorptivity at high temperature [50], which is about 0.9, ray scattering has been neglected and therefore their reflection is considered specular.
3- The voxels corresponding to the fluid are considered to be voxels of air: we consider that the energy of the rays is not absorbed when they pass through these voxels.
4- The incidence angles of the rays can have a very wide range of values, depending on the modelling of the selected light source (here a heliostat).

4.2.3 Validation

Ray tracing code validation is based on the correspondence between the macroscopic extinction coefficient obtained experimentally on SiC foams, and that calculated by the code, on equivalent foams (same porosity and same average pore diameter).

Several formulas have been postulated, whether digitally or experimentally, to link the macroscopic extinction coefficient of SiC foams with their porosity and average pore diameter [51–54]. To validate the ray tracing code, we chose to refer to that provided by Hendricks and Howell [52] because it results from an experimental study on SiC foams with high absorptivity (0.9), like the manufactured SiC material produced in this work:

$$\beta = \frac{4.8}{d}(1-\varphi) \qquad 8$$

where β is the macroscopic extinction coefficient, d is the average pore diameter and φ is the porosity. This formula is valid only if the porosity is equal to 80% and if the average pore diameter varies between 0.6 and 2 mm. Thus, to respect the validity domain of the empirical formula (8), 6 virtual foams were generated (examples in Figure 8) with these two parameters:

- 80% porosity for each of them;
- An average pore diameter varying between 0.8 mm and 1.8 mm, with a step of 0.2 mm.

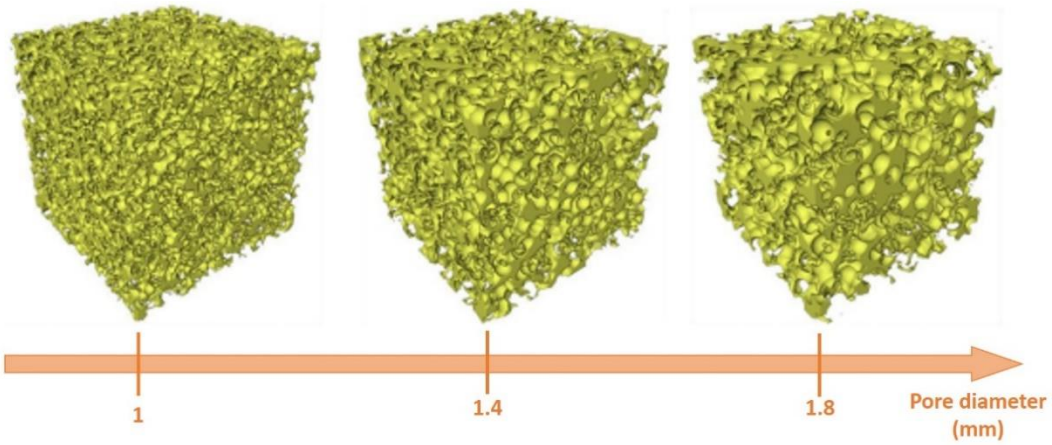

Figure 8: Example of three virtual foams made with 1200^3 voxels. Each of them has a porosity of 80%, a length of 2 cm and an increasing pore diameter.

The procedure to determine a digital macroscopic extinction coefficient in each virtual foam takes places in three steps: i) a simulation with the ray tracing code where rays are launched with a normal incidence angle to the front surface and where both front and rear faces have "free" boundary conditions (the four others have periodic boundary conditions). The absorptivity of the solid skeleton is taken at 0.9; ii) at the end of the simulation, formula (6) is applied to obtain the curve of the intensity of the incident flux transmitted ($I(z)$) throughout the depth (z); iii) a least squares method is used between the curve obtained in the previous step and the Beer-Lambert law $I(z) = I_0 e^{-\beta z}$ to determine the digital macroscopic extinction coefficient (I_0 is the intensity of the incident flux transmitted on the front face). Figure 9 shows the results obtained for each simulation on different virtual foams. They are very close to the experimental curve resulting from formula (8).

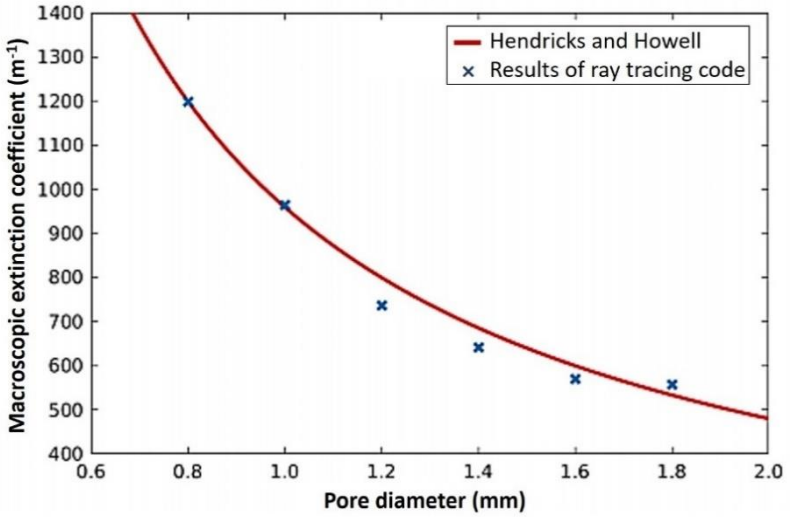

Figure 9: Result of the comparison between the extinction coefficients calculated for digital foams with 80% porosity and variable pore diameter and the relationship stated by Hendricks and Howell [52].

4.3 Heat transfer simulations

4.3.1 Computing code

The high temperatures reached in volumetric receivers led us to use a computing code coupling heat transfers by conduction and by radiation developed by Niezgoda et al. [1]. This code, where basic equations are widely described in the previous reference, is based on a discretisation by finite differences of the heat equation coupled with the Radiation Transfer Equation (RTE). For each voxel i, a flux balance equation can be written:

$$\sum_{k=1}^{6} \frac{2\delta\lambda_i\lambda_k}{\lambda_i+\lambda_k}(T_k - T_i) + \pi\delta^2 \sum_{k=1}^{6}(I_k^e - I_k^s) = 0 \qquad 9$$

Where k iterate on his six neighbours voxels, λ and T are respectively the thermal conductivity and the temperature (air or solid, depend of the nature of the voxel or his neighbour), δ is the size of a voxel, I^e is the inlet intensity on the k-face and I^s is the outlet intensity on the k-face. Two equations link these last two intensities. The first one, which indicates that the outlet intensity on the j-face of the voxel i is dependent on the inlet intensity of the five others faces of the voxel, is given by:

$$I_j^s = \sum_{k=1}^{5}(I_k^e - \mathrm{I}_i^0)F_k + I_i^0 \qquad 10$$

Where I_i^0 is the intensity of the blackbody (dependant on T) and F_k is a special form ratio with absorption. The second equation indicates, for a face j of the voxel i, that the inlet intensity is the sum of the transmitted intensity of the outlet intensity of the neighbour voxel (in contact with this j-face) and the reflected outlet intensity on this j-face of this voxel i:

$$I_j^e = \tau_k I_k^s + \rho_i I_i^s \qquad 11$$

Where τ_k and ρ_i are respectively the transmitivity on the face j of the neighbour k and the reflectivity on the face j of the voxel i.

The radiative boundary conditions of each voxel positionned at the boundaries are:

- If a flux ϕ_0 is imposed: $I_j^e = \phi_0$, where j is the boundary face;
- If a temperature T_{imp} is imposed: $I_j^e = \varepsilon I^0(T_{imp})$, where ε is the emissivity of the voxel

There are 13 unknowns per voxel (6 inlet intensities, 6 outlet intensities and the temperature). The problem can be simplified from thirteen to seven unknowns per voxel by injecting equations (9) into equations (10). In fact, the system to be solved is composed of 7xN unknowns (6 inlet intensities and the temperature), where N is the total number of voxel. For this study, this code was slightly modified in terms of the resolution of the matrix system. The 7xN unknowns of the problem are no longer determined by the minimisation of a single system, but rather by the iterative resolution of two coupled systems, one governing the 6xN intensities and the other governing the N temperatures. This modification made it possible on the one hand to decrease the computation time and, on the other hand, to deal with complex structures, such as those on which we wish to work, because this mathematical scheme is more stable, in particular in the case where air and solid temperatures are highly different.

4.3.2 Assumptions

Various assumptions are made in this thermal computing code:

1) The intensities are isotropic per half-space on each face of each voxel. Two intensities are therefore considered per face (front and back).
2) The properties and radiative quantities of each constituent are independent of the wavelength (grey medium). This amounts to considering average properties and radiative quantities. This assumption, which may seem to be a strong assumption, is nevertheless legitimate because the temperature field sought results from the consideration of energy quantities that integrate all of the contributions of each wavelength.
3) For a reason of calculating time-consuming, the thermophysical and radiative properties of air and solid are independent of the temperature. This point will be improved for future work.
4) The internal exchange coefficient between the solid/air interface is constant within the volume. The internal air reference temperature associated with the internal exchange coefficient is assumed to be the mean air temperature within the whole volume.

5 Results and discussion

5.1 Virtual structures generated

The three virtual structures resulting from the digital optimisation loop (see “General approach” and Figure 2) are shown in Figure 10. They are all cylindrical, measuring 5 cm in diameter and about 5 cm in depth. These dimensions correspond to the size of the samples imposed by the OPTISOL test bench.

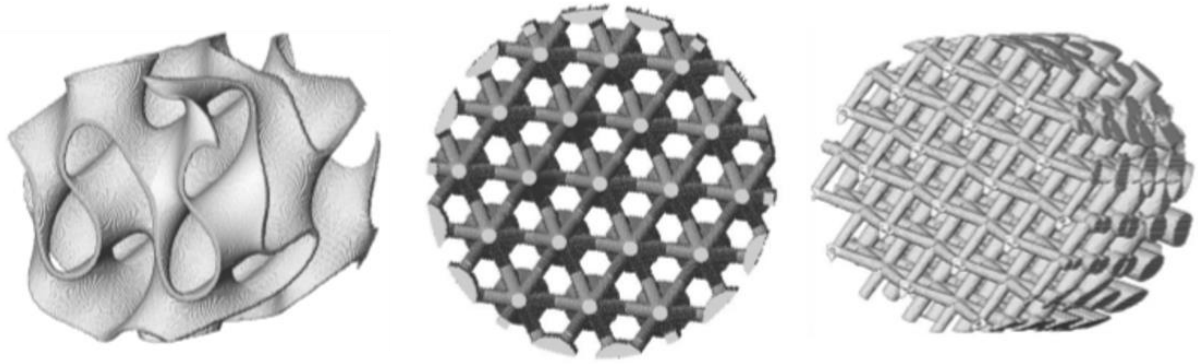

Figure 10: Three structures generated, with a voxel size of 167 µm. Left: Modified gyroid. Centre: Forest of cones. Right: Criss-crossed cones

The first is a modified TPMS (Triply Periodic Minimal Surface) structure. It was first generated according to the approximation of its surface equation given by [55]:

$$\sin(2\pi x)\cos(2\pi y) + \sin(2\pi y)\cos(2\pi z) + \cos(2\pi x)\sin(2\pi z) = 0 \qquad 12$$

where x, y and z are the coordinates of any point belonging to a Cartesian coordinates system and satisfying this equation. It then underwent two modifications. The first was an elongation along its depth; to achieve this, we replaced z in formula 12 with $z/2$. The second modification was a 45 ° rotation along one of the two axes perpendicular to the depth. Its wall thickness was 667 microns. This value corresponds to a compromise allowing a high specific surface area to be achieved, while retaining

the ability to produce the part with the ZPrinter 310+. Indeed, the size of the smallest achievable details is around 500 µm. Its volume surface area and its porosity are, respectively, 333.28 m^{-1} and 92.21%.

The second structure generated is a structure based on a "cone forest", and inspired by Olalde et al. [56]. Several cones, spaced apart, are staggered in space. They are all oriented perpendicular to the front face and oriented in such a way that their truncated apexes coincide with this face. In order to ensure a single-piece structure, cylindrical bars connect the neighbouring cones to each other, from the top of one to the centre of the base of the other. Due to its cone-based composition, this structure has a porosity gradient, from the front face (greater porosity) to the rear face (lower porosity). Its overall porosity is 71.63% and it has a volume surface area of 479.54 m^{-1}

The third structure studied is also composed of cones. These are regularly arranged in space, but for this geometry the axis of the cones is not perpendicular to the front face. They are oriented to criss-cross at different levels to form regular cells, the ligament section of which is increasingly higher with depth. This structure, also exhibiting a porosity gradient as a function of depth, can be assimilated with modification of the structures currently being studied (foams, honeycombs): it is composed of regular cells, but with different geometric characteristics depending on their depth. Its average porosity is 77.33%, and its volume surface area is 558.42 m^{-1}

5.2 Solar absorption and energy distribution

The ray tracing code, described above, was applied to the three virtual structures generated. For these three simulations, the numerical parameters were identical, and are summarised in Table 1.

Characteristics	Parameters
Light source shape	Conical
Light source opening half-angle	30°
Number of rays traced per voxel	32
Solid absorption	0.9
Boundary conditions	Free for the 6 faces

Table 1: Parameters used for ray tracing simulations

To comply with the conditions of the OPTISOL test bench, the light source chosen for these simulations was conical and had an opening half-angle of 30°. This source was, in addition, discretised into 32 rays per voxel. The solar absorptivity of the solid skeleton was set at 0.9, and therefore its solar reflectivity was 0.1 (no transmissivity). The boundary conditions were free for all 6 faces, which implies the rays are not reintegrated into the domain (by reflection or by periodicity) once they reach one of these 6 faces.

The intensity of the incident flux transmitted (formula 6) through the three structures is shown in Figure 11. For comparison, the curve of the intensity of the incident flux transmitted in a foam with 80% porosity and a pore diameter equal to 2 mm is plotted. This foam was generated with the numerical tools described above, and the result is consistent with Chen et al. [57]. The three complex geometries exhibit a much lower extinction rate than the foam curve in the inlet zone (between 1 and 2 cm depth, see Figure 11), but this rate is still higher than the ideal curve. And, after this zone, the extinction rate drastically decreases to a constant transmissivity value due to the presence of holes at the end of the sample geometry.

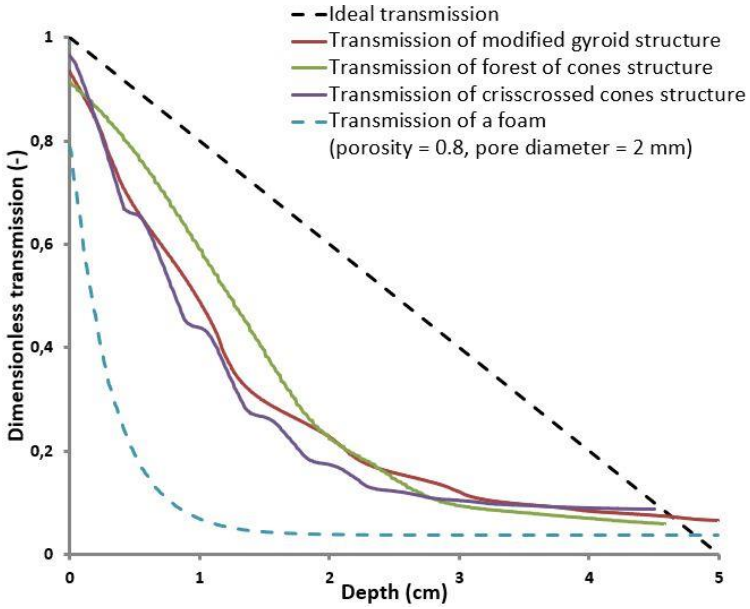

Figure 11: Simulation results on the three virtual structures generated. Dotted lines: ideal transmission curve. Full lines: dimensionless transmission calculated for the three structures.

For the modified Gyroid structure, extinction skips are almost non-existent due to the geometric continuity of the structure. However, absorption on the front face is not negligible (approximately 10% of the total flux), as evidenced by the drop in transmission at zero depth. To improve this point, it would have been necessary to decrease the volume of solid on the front face, but that would certainly have been problematic for manufacturing. Transmission through the rear face is high (about 8% of the total flux), because this structure is very porous. A fairly significant loss of energy is expected during the characterisation in the OPTISOL test bench, which will necessarily affect the final energy yield.

The structure organised into a cone forest presents a smooth extinction of solar radiation along the depth due to the continuous cone structure. In addition, transmission through the rear face, of approximately 5% of the incident solar flux, is a low value, which makes this structure efficient with respect to solar absorption. However, its weakest point is the absorption on the front face, of approximately 8% of the incident solar flux, due to the truncation of the cone tips.

The transmissivity curve of the criss-crossed structure exhibits extinction skips due to the regular position of the strut connections and transmission through the rear face is weak (about 5% of the incident solar flux)

5.3 Thermal distribution

After analysing the transmissivity curves for these three structures, the thermal distribution induced by solar absorption was modelled. Simulations with the thermal computing code presented above were carried out.

The energy distribution in each voxel, expressed as thermal flux (W/m²), becomes a source term for this computation. The material properties used are shown in Table 2.

Properties	Air/Solid	Values
Thermal conductivity $W.m^{-1}.K^{-1}$	Air	0.06
	SiC	15
Absorption coefficient m^{-1}	Air	0
	SiC	Imposed to have an absorptivity of 0.9
Extinction coefficient m^{-1}	Air	0
	SiC	Imposed to have an emissivity of 0.9
Complex optical index component	Air	n=1; k= 0
	SiC	n=2.58; k=0.005
Internal convection coefficient – $W.m^{-2}.K^{-1}$		100 - 150

Table 2: Properties of the materials used for thermal computations

The complex optical index of the solid was found in [58] and assumed independent of temperature. Absorptivity and emissivity, as well as that of the thermal conductivity of the solid, also independent of temperature, come from [50], which lists some properties of the SiC material that we manufactured (3D printing by binder jetting, thermal treatments, plaster elimination, SMP-10 infiltration, CVI and then CVD). The heat exchange coefficient by convection is constant within the structure for an airflow at 1 g/s [59]. All these values were taken for a temperature of 873K.

The boundary conditions are as follows:

- Four lateral faces: adiabatic for solid and air phases.
- Front face: air temperature is imposed at 293 K and a convection condition is assumed for the solid (exchange coefficient equal to 10 $W/m^2/K$, air reference temperature equal to 293 K).
- Rear face: a convection condition is assumed for the solid (exchange coefficient equal to 10 $W/m^2/K$, air reference temperature equal to the air on this same face, and therefore determined iteratively).

Result simulations

Two simulations were carried out on each structure: one with an internal convection coefficient of 100 $W.m^{-2}.K^{-1}$, and another with an internal convection coefficient of 150 $W.m^{-2}.K^{-1}$. The results of the thermal simulations, with an internal convection coefficient of 100 $W.m^{-2}.K^{-1}$, are shown in Figure 12. For each structure, either air or solid temperature profiles have the same behaviour. The curves increase to a maximum, located at a depth of about 1 cm for the air and about 0.5 cm for the solid, then decrease to the rear face. The rise in the temperature curve of the solid close to the front face of the receiver is significant of a gradual absorption of the solar flux, tending towards the beginning of a volumetric effect. However, the following decrease is significant of a strong absorption in the zone where the maximum temperature is located, thus preventing the volume effect from being established.

For the forest of cones structure, the solid temperature curve is smooth because there are no absorption skips of the solar flux, as shown in Figure 11. At the rear face, for an internal convection coefficient of 100 $W.m^{-2}.K^{-1}$, the solid temperature is equal to 1272 K and the air temperature is equal to 1227 K. For an internal convection coefficient of 150 $W.m^{-2}.K^{-1}$, these temperatures are respectively equal to 1222 K and 1189 K.

For the criss-crossed cones structure, the solid temperature curve is broken where the absorption of the solar flux included skips (see Figure 11). At the rear face, for an internal convection coefficient of

519 100 $W.m^{-2}.K^{-1}$, air and solid temperatures are very close and are respectively equal to 1183 K and 1181
520 K. For an internal convection coefficient of 150 $W.m^{-2}.K^{-1}$, these temperatures are respectively equal
521 to 1175 K and 1174 K.

522 For the modified gyroid structure, the solid temperature curve is discontinuous, and a plateau is
523 present between 0.45 cm and 1.15 cm in depth. Unlike the criss-crossed cones structure, they are not
524 due to solar flux absorption skips (see Figure 11). Initially, the gyroid structure is periodic and its
525 volume fraction is constant throughout the depth. However, in this work, it was rotated with respect
526 to an axis perpendicular to the depth, thus making this structure non-periodic and with a volume
527 fraction not evolving linearly or constantly with depth. In addition, since the structure is thin, the
528 temperature distribution over a slice of the depth can be very scattered. At the rear face, for an internal
529 convection coefficient of 100 $W.m^{-2}.K^{-1}$, the solid temperature is equal to 1170 K and the air
530 temperature is equal to 1208 K. For an internal convection coefficient of 150 $W.m^{-2}.K^{-1}$, these
531 temperatures are respectively equal to 1147 K and 1177 K.

532

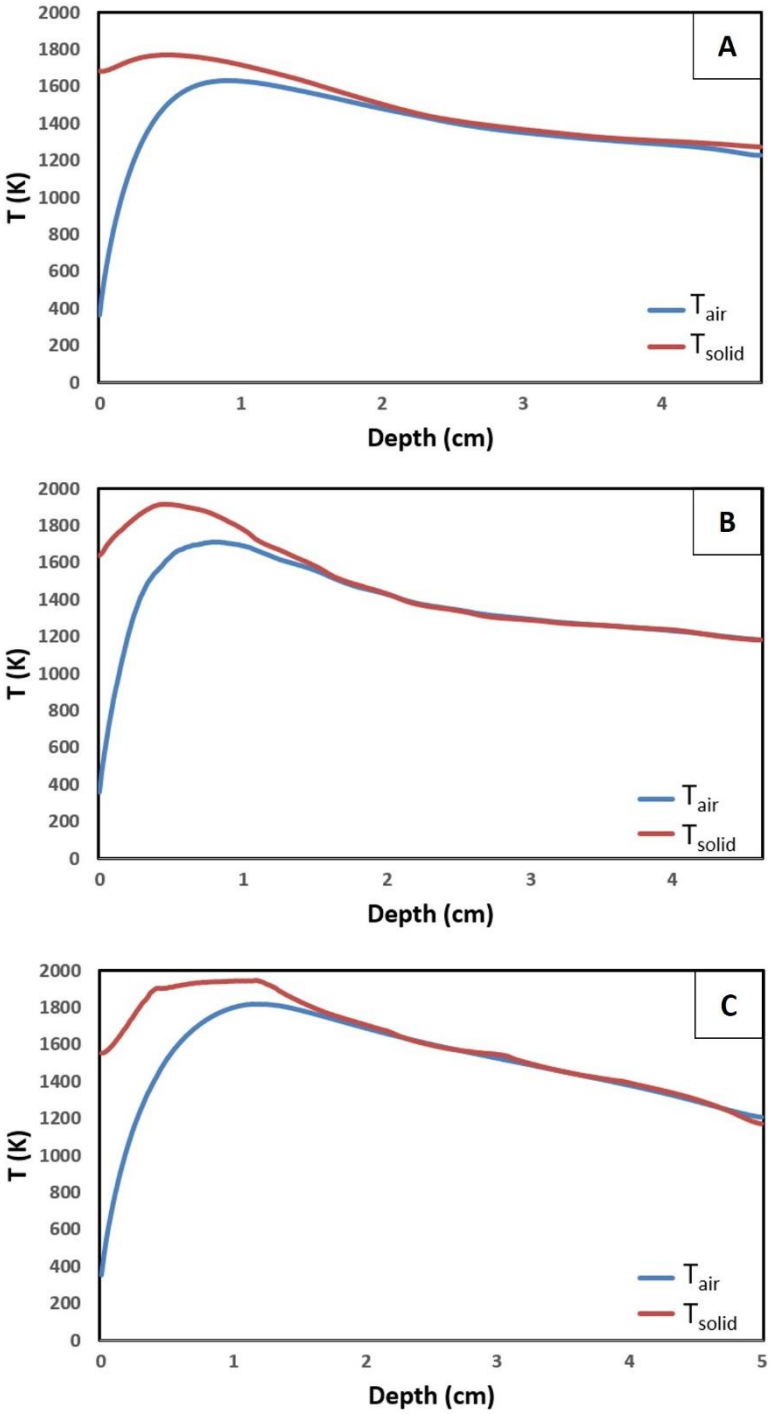

Figure 12: Results of thermal simulations on the 3 virtual structures, for an internal convection coefficient of 100 W.m^{-2}.K^{-1}. A: Forest of cones structure. B: Criss-crossed cones structure. C: Modified gyroid structure.

5.4 Manufacturing

The three structures were produced by the process described in Part III. The structures are shown in Figure 13 at two different stages: before reinforcement by CVI/CVD and after. A 3D microscope image was also produced after the reinforcement stage, on the one hand in order to measure the thickness of the ligaments at the end of the process and, on the other hand, to observe the surface finish. For the three structures, the surface shows a granular appearance despite the CVD post-treatment, which must limit the “staircase” effect due to the layer-by-layer manufacture of the part. Compared to the theoretical models, the wall thickness of the structures is approximately 100 to 150 µm greater,

reflecting the difficulty in mastering the entire production chain, which combines various processes (additive manufacturing and CVI/CVD).

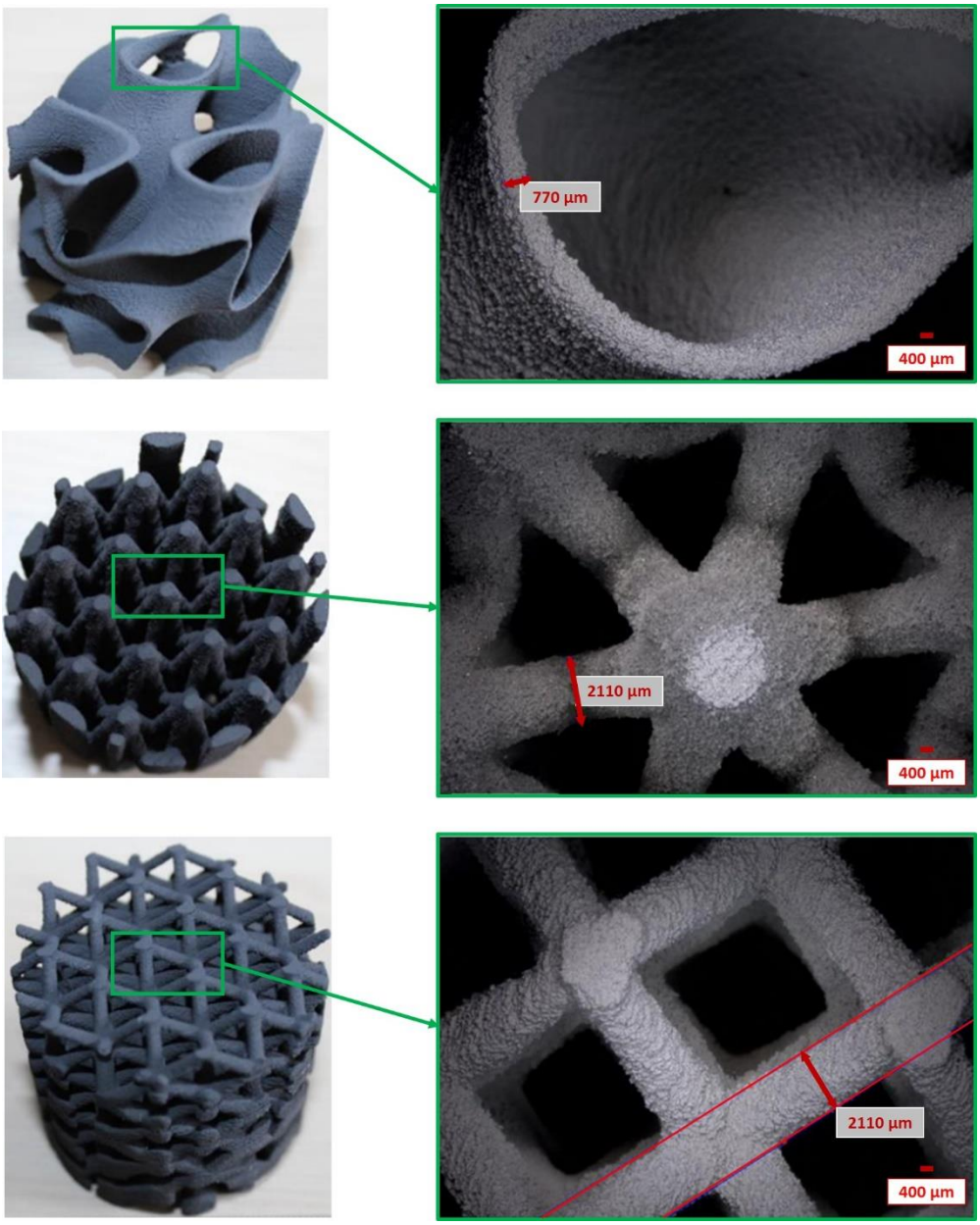

Figure 13: Three printed structures. From top to bottom: Modified gyroid, forest of cones and criss-crossed cones. On the left: after CVI / CVD reinforcement. On the right: 3D microscope images (after reinforcement) showing the surface finish and thickness of the ligaments.

The structure organised into a cone forest suffered some damage at the most fragile locations of its perimeter during the post-treatment stages. However, the consequences with regard to the solar flux absorption are minimal, since this damage is located at the edges.

5.5 Tests on the OPTISOL test bench

The structures, once manufactured, were tested on the OPTISOL test bench (Table 3). For each structure, the tests were carried out with a mass flow of 1 g/s. The energy efficiency η was calculated using the following formula, where T_{air}^{in} is the air temperature at the inlet, equal to 293 K:

$$\eta = \frac{\varphi_{inc}}{\dot{m} C_p \left(T_{air}^{out} - T_{air}^{in}\right)} \qquad 13$$

φ_{inc} is the incident flux, measured for each test, $\dot{m}$ is the mass flow of air, C_p is the specific heat of air and T_{air}^{out} is the outlet air temperature, measured at the outlet of the tested sample. The values of the incident flux, lateral losses and the outlet temperature determined digitally (for comparison) are also indicated in this table.

Structure	φ_{inc}	Lateral losses	η	T_{air}^{out} (experimental)	T_{air}^{out} (numerical)
	kW/m²	kW/m²	-	K	K
Modified gyroid	944	178	0.47	1098	[1177 – 1208]
Forest of cones	942	146	0.49	1133	[1189 – 1227]
Criss-crossing cones	928	199	0.44	1038	[1175 – 1183]

Table 3: Results of tests carried out on the OPTISOL test bench for the three printed structures. Numerical values obtained after thermal simulations are also given for comparison.

Experimental tests show outlet air temperatures between 1038 K and 1133 K and energy yields between 0.44 and 0.49. Among these three structures, the best performances were obtained for the forest of cones structure. This is explained by the fact that this structure offers the best compromise between porosity (for uniform absorption in depth) and volume surface area (for greater local convective exchanges). Conversely, the structure with the worst performance was the criss-crossed cones structure. This structure, with a greater surface area than the other two, absorbs the incident solar flux very quickly (the volume of the structure is not well exploited, see Figure 11). It can also be noted that, for the three structures, lateral losses were very significant: they can represent up to around 20% of the incident solar flux. These losses are mainly due to conduction through the insulation in contact with the cooled optical homogeniser, which acts as a heat sink (producing a heat flux through the insulation). These losses were monitored by using the cooled homogenizer as a calorimeter which was previously calibrated on-sun without the sample holder and the heated insulation.

Mey-Cloutier et al. [16] performed similar tests on the same setup, but with SiC foams having higher specific surface area. For an incident solar flux of 884 kW/m² and a mass air flow rate equal to 1 g/s, they reported a temperature of the exiting air of 1271 K, for an energy efficiency of 0.59. The lower values of the temperatures of outlet air and energy yields recorded in this study may be explained by the following three points:

1) The specific surface area is too small in the inlet zone leading to weak convective exchanges.
2) Not all the incident solar flux is intercepted by the geometry, it is either absorbed by the sample holder lateral walls (due to high porosity of the samples) or transmitted.
3) The lateral losses are considerable.

The comparison between the experimental and the numerical outlet temperature shows an important difference (103.5 K on average). The principal reasons are the large thermal losses through the lateral walls of the sample holder and the approximation of the convective heat transfer where both the

internal exchange coefficient and the associated internal air reference temperature have been set at a constant value. For a more precise numerical result, fluid dynamics must be modelled in future works. Nevertheless, numerical hierarchy between the outlet air temperature for the three structures is the same as the experimental hierarchy.

Images of the front face of the structures provided by the thermal camera during the tests (Figure 14, at the top) and pictures of the structures after the tests (Figure 14, centre) confirm that the temperatures computed are relevant (Figure 14, bottom).

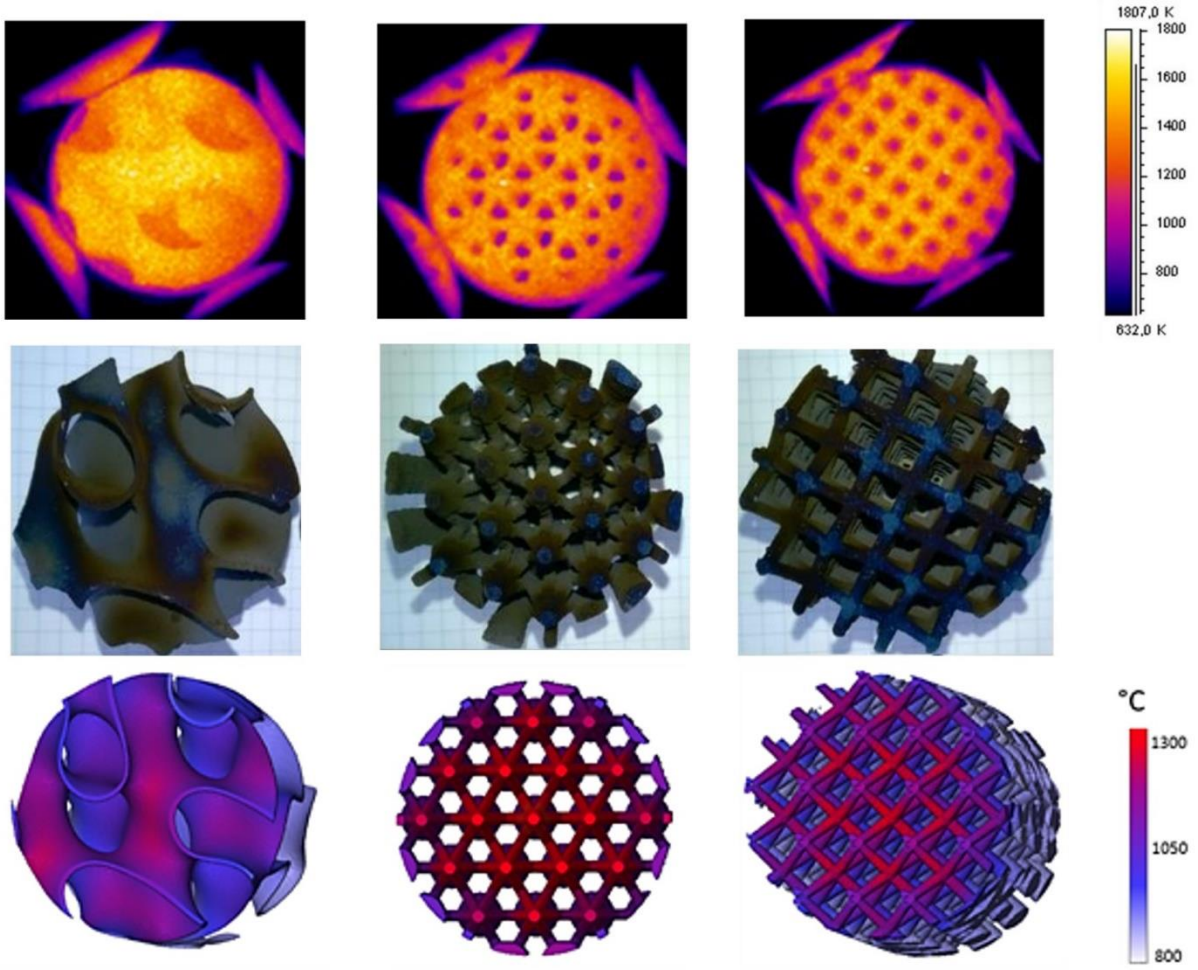

Figure 14: Top: black body equivalent temperature images at the front for an air flow equal to 1 g/s. Centre: Pictures of the structures after the tests. Bottom: Numerical results. From left to right: modified gyroid structure, forest of cones structure and criss-crossed cones structure.

The pictures of the three structures after testing show a blue iridescent layer formed where the maximum values are reached numerically. Analysis by electron probe microanalyser of a printed sample subjected to the same exposure conditions as on the OPTISOL bench (Figure 15), shows an oxidised silica (SiO_2) layer formed after air has passed through the hottest parts of the structures.

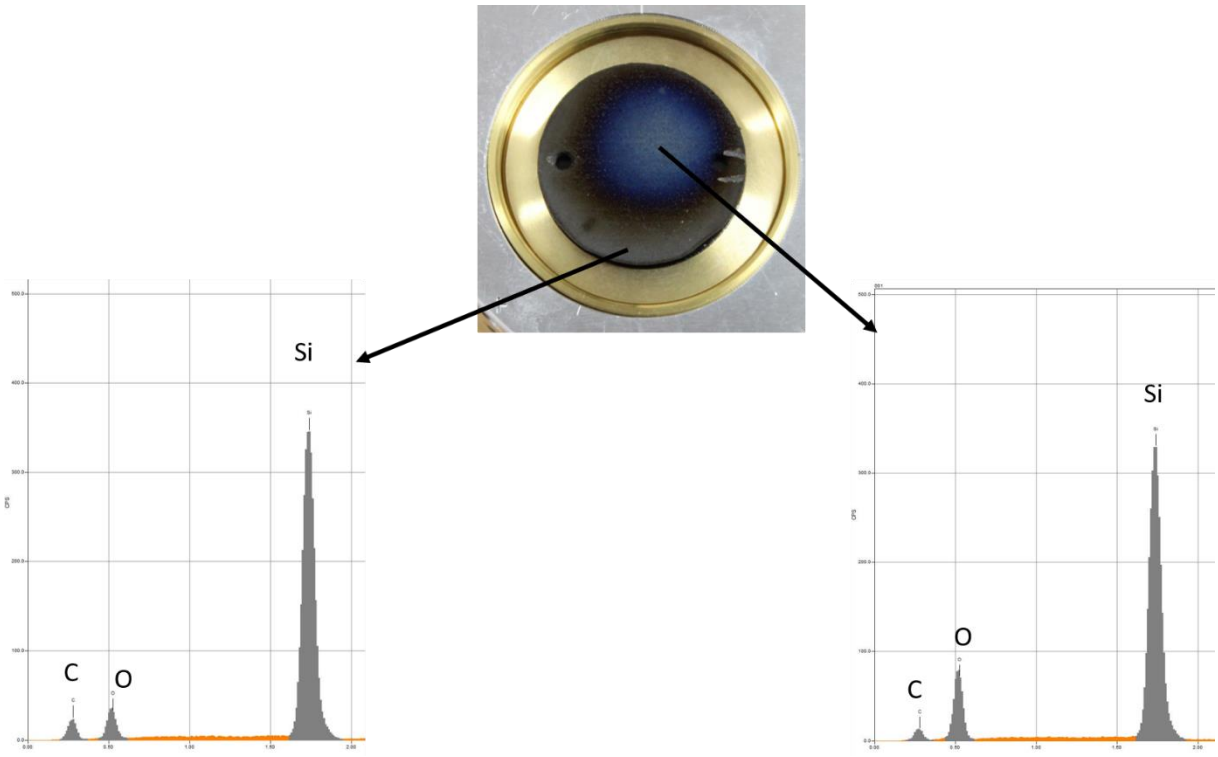

Figure 15: Electron probe microanalyses of a sample manufactured by the same process sequence as the structures. Left, analysis of a non-bluish area; Right, analysis of a bluish area (oxidation layer).

6 Conclusions and perspectives

This work demonstrates that digital material engineering methodology is promising for optimising a ceramic architecture. Following the application of this approach to high temperature volumetric STPP receivers, it has been shown that new geometries, made of SiC and with complex shapes, can be manufactured by 3D printing (binder jetting).

After numerical structure optimisation, performed using an iterative loop between the generation of the structures and ray tracing, 3 structures were printed and tested on the OPTISOL test bench of the PROMES laboratory. In parallel with the experimental tests, conductive-radiative simulations, without modelling of the fluid dynamics, were carried out on these 3 structures, in order to compare the numerical and experimental results. Despite the presence of large experimental losses, the comparison shows that the numerical results are in acceptable agreement with the experimental values.

The experimental tests highlighted the following points:

- The material manufactured by 3D printing withstands the conditions of high temperature volumetric receivers.
- A layer of silica formed at the hottest parts of the structure.
- The performances of these new geometries are lower than those of the conventional foams normally used because they had an insufficient specific surface area, even if the temperatures of the outlet air reached a maximum of 1133 K.

These first results are very encouraging, since it is recommended to have an air temperature at the outlet of the receiver above 750°C [60]. However, the receiver efficiency must be greater than 75%, which was not achieved in this study (maximum 49%). Thus, improvements to the receiver shape and the digital model should be implemented in future work.

In terms of the shape of the receiver, in a general manner, it would be interesting to generate structures that are closed on the sides to limit lateral losses and with a higher specific surface area. This last point can be solved by the generation of new geometries and/or by manufacturing using stereolithography. This process would make it possible to manufacture structures with higher resolution and therefore increase their specific surface area.

In terms of material, it is possible to modify the SiC/plaster ratio of the initial powder. This would make it possible to obtain a final material with a different microstructure comprising more or less residual porosity. The thermal and optical properties would be modified, thus implying different solar absorption and thermal distributions.

In terms of simulation, to fully optimise the structures, i.e. comprising thermal simulations in the optimisation loop, thermal simulations must be coupled with fluid dynamics to have a local internal exchange coefficient, and not constant such as in this study. This will therefore result in more precise results.

References

[1] M. Niezgoda, D. Rochais, F. Enguehard, B. Rousseau, P. Echegut, Modeling heat transfer within porous multiconstituent materials, Journal of Physics: Conference Series. 369 (2012). https://doi.org/10.1088/1742-6596/369/1/012001.

[2] P. David, T. Piquero, J. Martegoutte, F. Schuster, Matériau céramique composite particulaire, pièce le comprenant, et procédé de préparation de cette pièce, 3074171A1, 2017.

[3] M. Pelanconi, E. Rezaei, A. Ortona, Cellular ceramic architectures produced by hybrid additive manufacturing: a review on the evolution of their design, Journal of the Ceramic Society of Japan. 128 (2020) 595–604. https://doi.org/http://doi.org/10.2109/jcersj2.2007.

[4] A.L. Ávila-Marín, Volumetric receivers in Solar Thermal Power Plants with Central Receiver System technology: A review, Solar Energy. 85 (2011) 891–910. https://doi.org/https://doi.org/10.1016/j.solener.2011.02.002.

[5] C.K. Ho, B.D. Iverson, Review of high-temperature central receiver designs for concentrating solar power, Renewable and Sustainable Energy Reviews. 29 (2014) 835–846. https://doi.org/https://doi.org/10.1016/j.rser.2013.08.099.

[6] F. Gomez-Garcia, J. González-Aguilar, G. Olalde, M. Romero, Thermal and hydrodynamic behavior of ceramic volumetric absorbers for central receiver solar power plants: A review,

Renewable and Sustainable Energy Reviews. 57 (2016) 648–658. https://doi.org/https://doi.org/10.1016/j.rser.2015.12.106.

[7] C.K. Ho, Advances in central receivers for concentrating solar applications, Solar Energy. 152 (2017) 38–56. https://doi.org/https://doi.org/10.1016/j.solener.2017.03.048.

[8] J.-F.P. Pitot de la Beaujardiere, H.C.R. Reuter, A review of performance modelling studies associated with open volumetric receiver CSP plant technology, Renewable and Sustainable Energy Reviews. 82 (2018) 3848–3862. https://doi.org/https://doi.org/10.1016/j.rser.2017.10.086.

[9] S. Alexopoulos, B. Hoffschmidt, Advances in solar tower technology, Wiley Interdisciplinary Reviews: Energy and Environment. 6 (2017) e217. https://doi.org/10.1002/wene.217.

[10] O. Behar, A. Khellaf, K. Mohammedi, A review of studies on central receiver solar thermal power plants, Renewable and Sustainable Energy Reviews. 23 (2013) 12–39. https://doi.org/https://doi.org/10.1016/j.rser.2013.02.017.

[11] M. Boehmer, M. Becker, M. Sanchez, Development of Volumetric Air Receivers, (1991).

[12] T. Fend, High porosity materials as volumetric receivers for solar energetics, 2010.

[13] B. Hoffschmidt, F.M. Téllez, A. Valverde, J. Fernández, V. Fernández, Performance evaluation of the 200-kWth HiTRec-II open volumetric air receiver, Journal of Solar Energy Engineering, Transactions of the ASME. 125 (2003) 87–94. https://doi.org/10.1115/1.1530627.

[14] J. Karni, A. Kribus, R. Rubin, P. Doron, The “Porcupine”: A Novel High-Flux Absorber for Volumetric Solar Receivers, Journal of Solar Energy Engineering. 120 (1998) 85–95. https://doi.org/10.1115/1.2888060.

[15] M. Böhmer, C. Chaza, The ceramic foil volumetric receiver, Solar Energy Materials. 24 (1991) 182–191. https://doi.org/https://doi.org/10.1016/0165-1633(91)90058-S.

[16] S. Mey-Cloutier, C. Caliot, A. Kribus, Y. Gray, G. Flamant, Experimental study of ceramic foams used as high temperature volumetric solar absorber, Solar Energy. 136 (2016) 226–235. https://doi.org/10.1016/j.solener.2016.06.066.

[17] A. Kribus, H. Ries, W. Spirkl, Inherent Limitations of Volumetric Solar Receivers, Journal of Solar Energy Engineering. 118 (1996) 151–155. https://doi.org/https://doi.org/10.1115/1.2870891.

[18] H.W. Price, D.D. Whitney, H.I. Beebe, SMUD Kokhala Power Tower Study, (1997).

[19] M. Posnansky, T. Pylkkänen, Development and testing of a volumetric gas receiver for high-temperature applications, Solar Energy Materials. 24 (1991) 204–209. https://doi.org/https://doi.org/10.1016/0165-1633(91)90060-X.

[20] W.E.C. Pritzkow, Pressure loaded volumetric ceramic receiver, Solar Energy Materials. 24 (1991) 498–507. https://doi.org/https://doi.org/10.1016/0165-1633(91)90086-Z.

[21] M. Becker, Th. Fend, B. Hoffschmidt, R. Pitz-Paal, O. Reutter, V. Stamatov, M. Steven, D. Trimis, Theoretical and numerical investigation of flow stability in porous materials applied as volumetric solar receivers, Solar Energy. 80 (2006) 1241–1248. https://doi.org/https://doi.org/10.1016/j.solener.2005.11.006.

[22] G. Barreto, P. Canhoto, M. Collares-Pereira, Parametric analysis and optimisation of porous volumetric solar receivers made of open-cell SiC ceramic foam, Energy. 200 (2020). https://doi.org/10.1016/j.energy.2020.117476.

[23] T. Fend, B. Hoffschmidt, R. Pitz-Paal, O. Reutter, P. Rietbrock, Porous materials as open volumetric solar receivers: Experimental determination of thermophysical and heat transfer properties, Energy. 29 (2004) 823–833. https://doi.org/10.1016/S0360-5442(03)00188-9.

[24] S. Du, M.J. Li, Q. Ren, Q. Liang, Y.L. He, Pore-scale numerical simulation of fully coupled heat transfer process in porous volumetric solar receiver, Energy. 140 (2017) 1267–1275. https://doi.org/10.1016/j.energy.2017.08.062.

[25] A. Kribus, Y. Gray, M. Grijnevich, G. Mittelman, S. Mey-Cloutier, C. Caliot, The promise and challenge of solar volumetric absorbers, Solar Energy. 110 (2014) 463–481. https://doi.org/10.1016/j.solener.2014.09.035.

[26] Z. Wu, C. Caliot, G. Flamant, Z. Wang, Coupled radiation and flow modeling in ceramic foam volumetric solar air receivers, Solar Energy. 85 (2011) 2374–2385. https://doi.org/10.1016/j.solener.2011.06.030.

[27] S. Luque, G. Menéndez, M. Roccabruna, J. González-Aguilar, L. Crema, M. Romero, Exploiting volumetric effects in novel additively manufactured open solar receivers, Solar Energy. 174 (2018) 342–351. https://doi.org/10.1016/j.solener.2018.09.030.

[28] C. Caliot, P.M. Déjardin, Numerical demonstration of the volumetric effect in a high specific surface absorber with Kelvin cells, in: AIP Conference Proceedings, American Institute of Physics Inc., 2019. https://doi.org/10.1063/1.5117523.

[29] M. Pelanconi, S. Zavattoni, L. Cornolti, R. Puragliesi, E. Arrivabeni, L. Ferrari, S. Gianella, M. Barbato, A. Ortona, Application of Ceramic Lattice Structures to Design Compact, High Temperature Heat Exchangers: Material and Architecture Selection, Materials 2021, Vol. 14, Page 3225. 14 (2021) 3225. https://doi.org/10.3390/MA14123225.

[30] M. Pelanconi, P. Colombo, A. Ortona, Additive manufacturing of silicon carbide by selective laser sintering of PA12 powders and polymer infiltration and pyrolysis, Journal of the European Ceramic Society. 41 (2021) 5056–5065. https://doi.org/10.1016/J.JEURCERAMSOC.2021.04.014.

[31] C. Pan, Y. Han, J. Lu, Design and Optimization of Lattice Structures: A Review, Applied Sciences 2020, Vol. 10, Page 6374. 10 (2020) 6374. https://doi.org/10.3390/APP10186374.

[32] O. Santoliquido, F. Camerota, A. Ortona, The influence of topology on DLP 3D printing, debinding and sintering of ceramic periodic architectures designed to replace bulky

738 components, Open Ceramics. 5 (2021) 100059.
739 https://doi.org/10.1016/J.OCERAM.2021.100059.

740 [33] T. Chartier, A. Badev, Rapid prototyping of Ceramics, Elsevier, 2013.
741 https://doi.org/10.1016/B978-0-12-385469-8.00028.9.

742 [34] Y. de Hazan, D. Penner, SiC and SiOC ceramic articles produced by stereolithography of
743 acrylate modified polycarbosilane systems, Journal of the European Ceramic Society. 37
744 (2017) 5205–5212. https://doi.org/10.1016/j.jeurceramsoc.2017.03.021.

745 [35] Z.C. Eckel, C. Zhou, J.H. Martin, A.J. Jacobsen, W.B. Carter, T.A. Schaedler, Additive
746 manufacturing of polymer-derived ceramics, Science. 351 (2016) 58–62.
747 https://doi.org/10.1126/science.aad2688.

748 [36] S. Li, W. Duan, T. Zhao, W. Han, L. Wang, R. Dou, G. Wang, The fabrication of SiBCN ceramic
749 components from preceramic polymers by digital light processing (DLP) 3D printing
750 technology, Journal of the European Ceramic Society. 38 (2018) 4597–4603.
751 https://doi.org/10.1016/j.jeurceramsoc.2018.06.046.

752 [37] J. Schmidt, P. Colombo, Digital light processing of ceramic components from polysiloxanes,
753 Journal of the European Ceramic Society. 38 (2018) 57–66.
754 https://doi.org/10.1016/j.jeurceramsoc.2017.07.033.

755 [38] E. Zanchetta, M. Cattaldo, G. Franchin, M. Schwentenwein, J. Homa, G. Brusatin, P. Colombo,
756 Stereolithography of SiOC Ceramic Microcomponents, Advanced Materials. 28 (2016) 370–
757 376. https://doi.org/10.1002/adma.201503470.

758 [39] Z. Fu, L. Schlier, N. Travitzky, P. Greil, Three-dimensional printing of SiSiC lattice truss
759 structures, Materials Science and Engineering A. 560 (2013) 851–856.
760 https://doi.org/10.1016/j.msea.2012.09.107.

761 [40] C. Polzin, D. Günther, H. Seitz, 3D Printing of Porous Al2O3 and SiC ceramics, Journal of
762 Ceramic Science and Technology. 6 (2015) 141–146. https://doi.org/10.4416/JCST2015-
763 00013.

764 [41] A. Zocca, C.M. Gomes, A. Staude, E. Bernardo, J. Günster, P. Colombo, SiOC ceramics with
765 ordered porosity by 3D-printing of a preceramic polymer, Journal of Materials Research. 28
766 (2013) 2243–2252. https://doi.org/10.1557/jmr.2013.129.

767 [42] S. Du, Z.Y. Li, Y.L. He, D. Li, X.Q. Xie, Y. Gao, Experimental and numerical analysis of the
768 hydraulic and thermal performances of the gradually-varied porous volumetric solar receiver,
769 Science China Technological Sciences. 63 (2020) 1224–1234. https://doi.org/10.1007/s11431-
770 020-1580-2.

771 [43] F. Gomez Garcia, J. Gonzalez-Aguilar, S. Tamayo-Pacheco, G. Olalde, M. Romero, Numerical
772 analysis of radiation attenuation in volumetric solar receivers composed of a stack of thin
773 monolith layers, in: Energy Procedia, Elsevier Ltd, 2014: pp. 457–466.
774 https://doi.org/10.1016/j.egypro.2014.10.199.

[44] Q. Zhu, Y. Xuan, Improving the performance of volumetric solar receivers with a spectrally selective gradual structure and swirling characteristics, Energy. 172 (2019) 467–476. https://doi.org/10.1016/j.energy.2019.01.166.

[45] S. Du, M.J. Li, Y. He, Z.Y. Li, Experimental and numerical study on the reflectance losses of the porous volumetric solar receiver, Solar Energy Materials and Solar Cells. 214 (2020). https://doi.org/10.1016/j.solmat.2020.110558.

[46] R. Sreeja, B. Swaminathan, A. Painuly, T. v. Sebastian, S. Packirisamy, Allylhydridopolycarbosilane (AHPCS) as matrix resin for C/SiC ceramic matrix composites, Materials Science and Engineering B: Solid-State Materials for Advanced Technology. 168 (2010) 204–207. https://doi.org/10.1016/j.mseb.2009.12.033.

[47] J. Yin, S.H. Lee, L. Feng, Y. Zhu, X. Liu, Z. Huang, S.Y. Kim, I.S. Han, The effects of SiC precursors on the microstructures and mechanical properties of SiCf/SiC composites prepared via polymer impregnation and pyrolysis process, Ceramics International. 41 (2015) 4145–4153. https://doi.org/10.1016/j.ceramint.2014.11.112.

[48] S.C. Zunjarrao, A. Rahman, R.P. Singh, Characterization of the evolution and properties of silicon carbide derived from a preceramic polymer precursor, Journal of the American Ceramic Society. 96 (2013) 1869–1876. https://doi.org/10.1111/jace.12273.

[49] S. Kaur, R. Riedel, E. Ionescu, Pressureless fabrication of dense monolithic SiC ceramics from a polycarbosilane, Journal of the European Ceramic Society. 34 (2014) 3571–3578. https://doi.org/10.1016/j.jeurceramsoc.2014.05.002.

[50] A. Baux, A. Goillot, S. Jacques, C. Heisel, D. Rochais, L. Charpentier, P. David, T. Piquero, T. Chartier, G. Chollon, Synthesis and properties of macroporous SiC ceramics synthesized by 3D printing and chemical vapor infiltration/deposition, Journal of the European Ceramic Society. 40 (2020) 2834–2854. https://doi.org/10.1016/j.jeurceramsoc.2020.03.001.

[51] B. Dietrich, T. Fischedick, S. Heissler, P.G. Weidler, C. Wöll, M. Kind, Optical parameters for characterization of thermal radiation in ceramic sponges - Experimental results and correlation, International Journal of Heat and Mass Transfer. 79 (2014) 655–665. https://doi.org/10.1016/j.ijheatmasstransfer.2014.08.023.

[52] T.J. Hendricks, J.R. Howell, Absorption / Scattering Coefficients and Scattering Phase Functions in Reticulated Porous Ceramics, Journal of Heat Transfer. 118 (1996) 79–87. https://doi.org/https://doi.org/10.1115/1.2824071.

[53] P.F. Hsu, J.R. Howell, Measurements of thermal conductivity and optical properties of porous partially stabilized zirconia, Experimental Heat Transfer. 5 (1992) 293–313. https://doi.org/10.1080/08916159208946446.

[54] Y. Zhao, G.H. Tang, Monte Carlo study on extinction coefficient of silicon carbide porous media used for solar receiver, International Journal of Heat and Mass Transfer. 92 (2016) 1061–1065. https://doi.org/10.1016/j.ijheatmasstransfer.2015.08.105.

812 [55] H.G. von Schnering, R. Nesper, Nodal surfaces of Fourier series: fundamental invariants of
813 structured matter, Z. Phys. B-Condensed Matter. 83 (1991) 407–412.
814 https://doi.org/10.1007/BF01313411.

815 [56] G. Olalde, G. Flamant, D. Schwander, C. Combescure, Advanced high temperature semi-
816 transparent solar absorbers, Solar Energy Materials. 12 (1985) 461–469.
817 https://doi.org/https://doi.org/10.1016/0165-1633(85)90039-5.

818 [57] X. Chen, X.L. Xia, H. Liu, Y. Li, B. Liu, Heat transfer analysis of a volumetric solar receiver by
819 coupling the solar radiation transport and internal heat transfer, Energy Conversion and
820 Management. 114 (2016) 20–27. https://doi.org/10.1016/j.enconman.2016.01.074.

821 [58] E.D. Palik, Handbook of Optical Constants of Solids - Google Livres, Academic Press, 1998.

822 [59] Z. Li, X. Xia, X. Li, C. Sun, Discrete vs. continuum-scale simulation of coupled radiation and
823 convection inside rectangular channel filled with metal foam, International Journal of Thermal
824 Sciences. 132 (2018) 219–233. https://doi.org/10.1016/j.ijthermalsci.2018.06.010.

825 [60] Y.L. He, Y. Qiu, K. Wang, F. Yuan, W.Q. Wang, M.J. Li, J.Q. Guo, Perspective of concentrating
826 solar power, Energy. 198 (2020) 117373. https://doi.org/10.1016/j.energy.2020.117373.

827

828